Journal of Raman Spectroscopy

WILEY

Journal of RAMAN SPECTROSCOPY

RESEARCH ARTICLE

Operando UV-Raman Spectroscopy Tracking the Evolving Intermediates in Hydrocarbon Conversion Over MFI Zeolites

Zixiao Jiang[1,2] | Jingfeng Han[1] | Yingxu Wei[1,3] | Zhongmin Liu[1,3]

[1]National Engineering Research Center of Lower-Carbon Catalysis Technology, Dalian Institute of Chemical Physics, Chinese Academy of Sciences, Dalian, China | [2]University of Chinese Academy of Sciences, Beijing, China | [3]State Key Laboratory of Catalysis, Dalian Institute of Chemical Physics, Chinese Academy of Sciences, Dalian, China

Correspondence: Jingfeng Han (jfhan@dicp.ac.cn) | Zhongmin Liu (liuzm@dicp.ac.cn)

Received: 10 June 2025 | **Revised:** 18 September 2025 | **Accepted:** 22 September 2025

Funding: We thank the National Key Research and Development Program of China (No. 2024YFB4105600), the National Natural Science Foundation of China (22172166, 22288101), the Youth Innovation Promotion Association CAS (2021182), the Clean Combustion and Low-Carbon Utilization of Coal, Strategic Priority Research Program of the Chinese Academy of Sciences (Grant No. XDA 29000000), and the Innovation Research Foundation of Dalian Institute of Chemical Physics, Chinese Academy of Sciences (DICP I202217) for the financial support.

Keywords: Brønsted acid sites | butene | methanol-to-olefins | UV-Raman spectroscopy | zeolite

ABSTRACT

Zeolites are widely used as catalysts in olefin conversion, methanol-to-hydrocarbons (MTH), and aromatics production. Brønsted acid sites (BAS) confined within zeolite frameworks critically facilitate olefin isomerization, oligomerization, cracking, and aromatization via carbocation-mediated mechanisms. However, the formation and evolution of intermediates, particularly under working conditions, remain challenging to observe. Here, we developed an *operando* system integrating 244-nm UV-Raman spectroscopy with gas chromatography and a multisampler, enabling simultaneous spectroscopic analysis and product quantification. We demonstrate that olefin adsorption mechanisms on zeolites depend on the Si/Al ratio and reaction temperature. Raman spectroscopy identified distinct adsorbed species: π-complexes (1640 cm^{-1}), olefinic carbocations (1615 cm^{-1}), and aromatic carbocations (1605 cm^{-1}). During 1-butene and methanol conversion, the transition from olefinic to aromatic carbocations depends on temperature. This study presents a Raman-based approach for the identification of BAS-stabilized carbocations in zeolites, offering mechanistic insights essential for the optimization of zeolite-catalyzed processes. The combination of Raman spectroscopy with online chromatography technology enables more comprehensive and reliable insights into the principles governing heterogeneous catalysis.

1 | Introduction

Zeolites—microporous aluminosilicates (or silicoaluminophosphates)—are widely employed in the chemical industry owing to their exceptional catalytic properties [1–3]. These materials play a central role in hydrocarbon transformation processes such as catalytic cracking, hydrocracking, and aromatization, where the catalysis from Brønsted acid sites (BAS) in zeolite frameworks drives reactivity [4–7]. Olefins (e.g., ethylene and propylene) and aromatics (e.g., benzene, xylene) are not only critical products in petrochemical processes but also serve as feedstocks for synthesizing high-value chemicals [8–10]. Furthermore, they act as key intermediates in hydrocarbon and methanol conversion reactions, enabling precise control over product distributions [11–14]. Understanding the mechanistic interplay between olefins and BAS—particularly during adsorption and catalytic

transformation—is essential for modulating the catalyst and optimizing industrial processes such as petroleum refining and chemical synthesis.

At low temperatures, olefins undergo isomerization and oligomerization over acid zeolite catalyst, complicating the interpretation of adsorption–desorption experiments. The interaction between olefins and BAS in zeolites is widely described as a two-step process: (i) initial formation of a π-complex (physisorbed state), where the π-electrons of the olefin double bond interact with BAS through hydrogen bonding to the acidic proton, followed by (ii) potential proton transfer to generate chemisorbed species [5, 15]. However, the identity of these chemisorbed intermediates remains contentious due to the scarcity of in situ characterization techniques. Proposed structures range from covalently bound alkoxy species (e.g., Si–O–C bonds) to carbocation-ion pairs (e.g., $[H\text{-}ZSM\text{-}5]^-$–$R^+$) [16, 17]. Furthermore, the catalytic mechanism of olefin conversion—particularly the role and evolution of adsorbed intermediates—remains unresolved, highlighting the need for advanced spectroscopic methods to track dynamic species under reaction conditions [18, 19].

Extensive studies combining experimental and theoretical approaches have explored olefin interactions with diverse zeolite catalysts [20–24]. Domen et al. observed stable π-complexes and double-bond isomerization during butene adsorption on H-ZSM-5 and mordenite at 230 K [25, 26]. In contrast, Lercher et al. [18] demonstrated that pentenes on ZSM-5 preferentially form alkoxy species rather than carbocations. Computational studies by Speybroeck et al. further revealed that carbocation stability depends on both olefin structure (e.g., butene vs. pentene) and temperature, highlighting the nuanced interplay of physicochemical factors [27]. While these works elucidate the complexity of olefin adsorption and transformation in zeolites, critical gaps persist: The reactivity of adsorbed intermediates under operando conditions remains ambiguous. Advancing in situ characterization techniques is essential to resolve these challenges and unify mechanistic understanding.

Among the various operando characterization techniques, Raman spectroscopy has emerged as a powerful tool for probing the evolution of hydrocarbon species on zeolite catalysts, owing to its direct sensitivity to skeletal vibrations of surface organics [28–30]. In particular, its strong response to C=C (and other conjugated) vibrational modes makes it especially suitable for identifying aromatics, olefins, and coke precursors, offering clear advantages over infrared spectroscopy, which is more effective in probing OH groups and zeolite framework vibrations [19, 31]. However, Raman studies of zeolite-catalyzed organic transformations often encounter challenges related to fluorescence effects [32, 33]. To overcome this limitation, Speybroeck et al. previously employed a unique Gaertner laser, which utilizes the latency of the fluorescence process to bypass this issue [34]. A more general strategy, however, is the use of deep-ultraviolet excitation (UV-Raman), which effectively suppresses fluorescence from aromatics and coke species and enables high-sensitivity, high signal-to-noise detection under complex flow reaction conditions. Beyond its superior anti-fluorescence capability, UV-Raman offers an intrinsic resonance enhancement effect ($\pi \rightarrow \pi^*$ transitions), greatly amplifying the spectral response of conjugated systems and carbocations, and thus allowing reliable detection of low-concentration and short-lived intermediates [35–37]. This advantage has been clearly demonstrated by Signorile et al., who systematically employed UV-Raman to identify aromatic and cyclopentadienyl conjugated intermediates in SAPO-34 and H-ZSM-5, thereby elucidating the aromatization pathways and stepwise accumulation of polyaromatic species during the methanol-to-hydrocarbons (MTH) process [28, 31, 38].

In this study, we established a 244-nm UV-Raman system coupled with gas chromatography to enable real-time tracking of the transformation of adsorbed hydrocarbon species on zeolites (Figure S1). To analyze the complex transformed gas products simultaneously, we employed a 16-position valve capable of storing up to 15 different reaction effluents at 15-s intervals for subsequent analysis. The simultaneous integration of in situ Raman spectroscopy and product analysis enables us to identify active intermediates and elucidate their reaction mechanisms. This system offers a novel approach to studying heterogeneous catalytic reactions, advancing mechanistic understanding of the transformation processes of surface organic species. This study aims to elucidate the adsorption behavior and catalytic conversion mechanisms of olefins (e.g., 1-butene) and methanol in MFI-type zeolites by developing an integrated platform *including operando* UV-Raman spectroscopy and real-time gas chromatography, enabling the comprehensive dissection of heterogeneous catalytic cycles spanning reactant adsorption, surface reactions, and product formation/desorption. Through systematic investigation of acidity modulation, butene adsorption, and conversion processes, we seek to unravel the interaction mode of olefins with BAS within zeolite channels, including the progression from physical adsorption states to π-complex formation, carbocation generation, and their subsequent transformation into olefins and aromatics. By correlating reaction temperature with carbocation speciation (allylic vs. aromatic) and related pathway (polymerization, cracking, and aromatization), we aim to establish structure–activity relationships between zeolite acidity (Si/Al ratio) and product distribution. These findings will deepen the molecular-level understanding of zeolite-catalyzed hydrocarbon transformations, providing theoretical foundations for optimized catalyst design and improved processes in the petroleum and chemical industries.

2 | Experimental Section

2.1 | Integrated System of Continuous-Flow UV-Raman With 16-Position GC Autosampler

Operando Raman spectroscopy was performed on a custom-built UV-Raman system integrated with online gas chromatography. The excitation source was a single-frequency 488-nm laser (Genesis CX488, Coherent) frequency-doubled to 244 nm by an external cavity doubler (Wavetrain, Spectra-Physics). The laser output (1 W) was attenuated to ~5 mW at the sample to avoid photodegradation. The beam was collimated and focused onto the catalyst bed using a set of quartz lenses. The scattered light was collected with a parabolic mirror, passed through a dichroic beam splitter and bandpass filters to suppress Rayleigh scattering, and then directed into a Shamrock 500i spectrograph (Andor) coupled

to a Newton DU940 CCD detector (Andor). The spectral resolution was ~2 cm^{-1}, with a typical acquisition time of 15 s per spectrum.

Reactions were carried out in a commercial in situ Raman cell (Xiamen Tuosi Technology Co. Ltd.) with a maximum heating rate of 20 $K \cdot min^{-1}$ and an operating limit of 873 K. The sample was loaded in a zirconia ceramic sample tube (4.5-mm diameter, 8-mm length) supported by quartz wool. The cell housing and windows were water-cooled to maintain stability and suppress excess vapor pressure of volatile feeds such as methanol.

To analyze the complex transformed gas products simultaneously, we employed a 16-position valve capable of storing up to 15 different reaction effluents at 15-s intervals for subsequent analysis. This setup ensured that Raman-detected surface intermediates could be directly correlated with GC-detected product distributions, providing true operando mechanistic insight.

2.2 | Catalyst Pretreatment

Before each operando UV-Raman measurement, the catalyst sample (0.02 g) was subjected to calcination in air at 600°C for 2 h. The system was subsequently purged with N_2 to remove residual O_2.

2.3 | Adsorption of 1-Butanol on MFI Zeolites

The temperature was stabilized at 25°C, and 1-butanol in N_2 gas (WHSV of 0.5 h^{-1}) was introduced. After 5 min, stop the 1-butanol injection and switch to directly introduce N_2 gas.

2.4 | Temperature-Programmed 1-Butene Conversion Reaction Over MFI Zeolites

The temperature was stabilized at 50°C, and 0.5% 1-butene in N_2 gas (WHSV of 0.5 h^{-1}) was introduced. After 10 min, the temperature was raised to 500°C at a rate of 10°C·min^{-1} and maintained. The gas mixtures were stored in a 16-position valve and then analyzed by an online gas chromatograph (Agilent GC 7890B).

2.5 | Methanol-to-Olefins (MTO) Reaction Over ZSM-5 Zeolites

When the temperature is stable, methanol in N_2 gas (WHSV of 0.5 h^{-1}) is introduced. The temperature-programmed experiment starts with cooling to 50°C; after 10 min, the temperature is raised to 600°C at a rate of 10°C·min^{-1} and maintained. The gas mixtures are stored in a 16-position valve and then analyzed by an online gas chromatograph (Agilent GC 7890B).

3 | Results and Discussion

3.1 | Properties of MFI Zeolites

The XRD patterns of the three zeolites used in this study exhibit same crystal structure, showing characteristic peaks at 7°–9° and 23°–24° (Figure S2), consistent with the MFI framework. The NH_3-TPD analysis reveals distinct acidity profiles for each zeolite (Figure S3). ZSM-5(38) exhibits two prominent desorption peaks at approximately ~230°C and ~450°C, corresponding to NH_3 adsorption at the weak and strong acid sites, respectively. In contrast, ZSM-5(100) displays two desorption peaks at ~200°C and ~410°C, with smaller peak areas than ZSM-5(38), indicating fewer weak/strong acid sites and lower overall acidity. The infrared spectra (Figure S4) reveal that in ZSM-5(38), the silanol band at ~3740 cm^{-1} is weaker, whereas the Brønsted acid hydroxyl band at ~3610 cm^{-1} is much more intense compared to ZSM-5(100), in good agreement with the NH_3-TPD results. In contrast, S-1 displays only the silanol band and virtually no BAS. For S-1, only minor desorption peaks are observed, confirming negligible BAS. These acidity differences correlate with Si/Al ratios: higher aluminum content results in the formation of more BAS. SEM images of S-1, ZSM-5(38), and ZSM-5(100) are presented in Figures S5–S7, respectively. The XRF analysis results of the three zeolites are presented in Tables S1–S3, which provide detailed information on their elemental composition and distribution.

3.2 | Adsorption of 1-Butene and 1-Butanol on MFI Zeolites

Figure 1 illustrates the operando Raman spectroscopic changes observed in zeolite catalysts with varying Si/Al ratios during the adsorption of 1-butene or 1-butanol at 50°C. A persistent Raman band at 2320 cm^{-1} is ascribed to the N_2 carrier gas signal (Figure S8). To mitigate laser power fluctuations, this band serves as an internal reference. Adsorption of 1-butene on MFI zeolites is marked by a dominant band at 1600–1640-cm^{-1} range, corresponding to C=C bond stretching vibrations [28, 35, 39]. Additional bands near 2900 cm^{-1}, linked to C-H bond stretching vibrations, are also observed [30]. Since S-1 lacks BAS, 1-butene adsorption on S-1 yields a physical adsorption band at 1636 cm^{-1} (Figures 1a and S9 black) [18, 40]. In contrast, ZSM-5(38) exhibits abundant BAS. The initial absorption band appears at 1640 cm^{-1} attributed to π-complexes [18, 25, 26], while after 180 s, a band at 1615 cm^{-1} emerges, coinciding with 2-butene detection in products, indicating double-bond isomerization. The dual Raman bands suggest two distinct adsorbed species (Figures 1b and S10). To validate these assignments, 1-butanol adsorption trials were conducted. On S-1, butanol remains inert in a molecularly adsorbed state, with a band at 1448 cm^{-1} attributed to methyl C–H vibrations (Figures 1c and S9 red) [39, 41]. No C=C stretching bands near 1600 cm^{-1} were observed, confirming no dehydration occurs. Conversely, ZSM-5(38) adsorption of 1-butanol generates a band at 1640 cm^{-1}, signaling dehydration to butene. Under N_2 purging, this band shifts to 1615 cm^{-1}, suggesting initial π-complex formation followed by carbocation generation. During butanol dehydration and butene isomerization, the tert-butyl carbenium ion serves as the crucial intermediate. Owing to its relative stability in the zeolite environment, this species promotes skeletal rearrangement, resulting in the generation of butene isomers [42, 43].

3.3 | Temperature-Programmed 1-Butene Conversion Reaction Over MFI Zeolites

When increasing the temperature of the 1-butene reaction over S-1 from 50 to 400 °C, Raman spectroscopy reveals a shifted

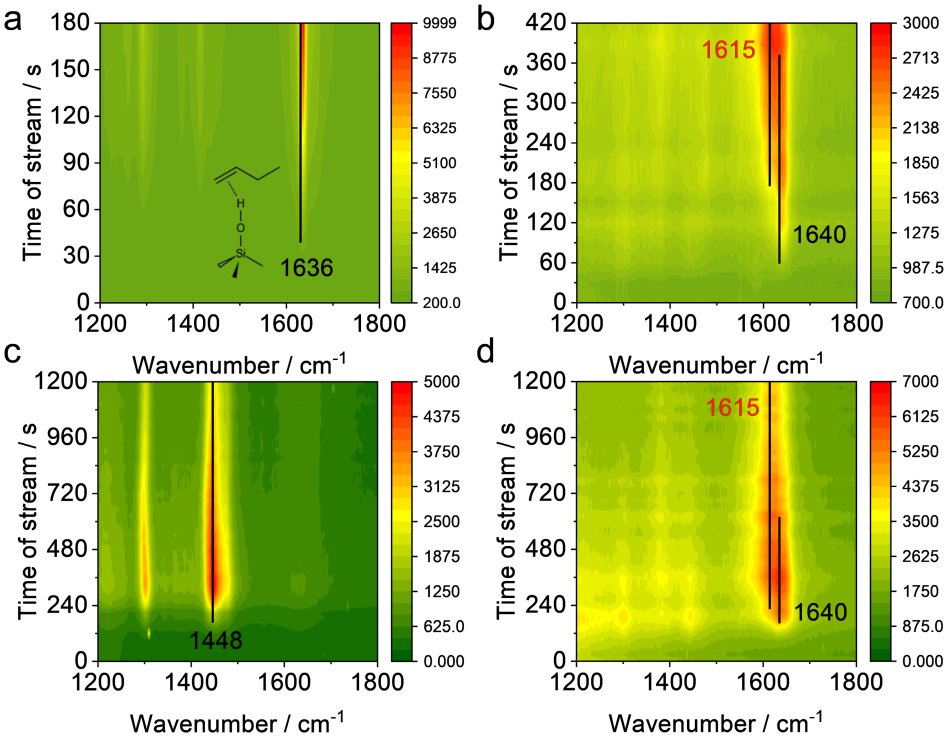

FIGURE 1 | The adsorption of 1-butene on S-1 and ZSM-5 (Si/Al = 38) is presented in panels (a) and (b), respectively, at 50°C. Similarly, the adsorption of 1-butanol on S-1 and ZSM-5 (Si/Al = 38) is shown in panels (c) and (d), respectively, at the same temperature.

band center at 1600 cm^{-1}, indicating aromatic compound formation (Figures 2a and S11) [43, 44]. Although only minor aromatic products are detected chromatographically, the intense 1600-cm^{-1} band demonstrates Raman spectroscopy's exceptional sensitivity and low detection limit for aromatic species. At lower temperatures (50°C–150°C), gas chromatography identifies only trace 2-butene (Figure 2b,c), indicating limited isomerization occurrence. The absence of BAS on S-1 restricts 1-butene to physical adsorption, as evidenced by the sharp 1636-cm^{-1} band attributed to adsorbed species. As temperature increases from 50°C to 150°C, this band attenuates markedly, with less than 10% 1-butene conversion. Simultaneously, double-bond isomerization occurred at 150°C, increasing the proportion of 2-butene and causing a red shift of the 1636-cm^{-1} band toward lower wavenumbers. Throughout the studied temperature range, the lack of BAS in S-1 suppresses propylene selectivity in oligomerization and cracking pathways, leaving double-bond isomerization as the dominant reaction.

Unlike S-1, ZSM-5(100)—which shares the MFI framework but contains BAS—enables chemisorption of 1-butene. Upon adsorption initiation, a Raman band appears at 1640 cm^{-1} (Figures 2d and S12), similar to physical adsorption band of 1-butene on S-1, suggesting dominate spectral differences stemming from acidity. Gas chromatographic analysis reveals 60% 1-butene conversion to 2-butene at 50°C (Figure 2e,f). At 175°C, polymerization initiates with C_5^+ formation, accompanied by attenuation of the 1640-cm^{-1} band and intensification of the 1615-cm^{-1} band, alongside a redshift. Gas chromatographic analysis revealed the formation of C_5^+ products, which can be attributed to the oligomerization of 1-butene followed by subsequent cracking, accompanied by minor amounts of propylene. During this process, the Raman features of higher olefins overlap with those of 1-butene, making it difficult to unambiguously distinguish polymeric species from monomeric olefins by Raman spectroscopy. Such species may manifest in UV-Raman spectra as broadened C=C stretching bands, which at elevated temperatures undergo further cracking to produce light olefins and aromatics. By 225°C, near-complete 1-butene conversion yields isobutene, propylene, and C_5^+ products, with the 1640-cm^{-1} band fully disappearing and the spectral center shifting to 1615 cm^{-1} (Figure 2d,e). To decouple isomerization effects, isobutene adsorption on ZSM-5(100) at 50°C produced a distinct 1615-cm^{-1} band (Figure S15), contrasting the 1640-cm^{-1} signal of physisorbed species. Computational studies confirm the tert-butyl carbocation is more stable than π-complexes or alkoxy species at room temperature [27], aligning the 1615-cm^{-1} band with this intermediate. However, contributions from other carbocations at this wavenumber cannot be excluded. At 350°C, the 1615-cm^{-1} band diminishes while the 1605 cm^{-1} intensifies, coinciding with reduced C_5^+ products, increased propane, and aromatic generation. Despite aromatics formation, the low BAS density favors cracking over aromatization, resulting in limited aromatic yields.

The product distribution from butene conversion over ZSM-5(38) is highly complex (Figure 2g–i). Upon initial adsorption, Raman bands at 1640 and 1615 cm^{-1} appear (Figure 2g), mirroring the behavior observed on ZSM-5(100). At 50°C, 71% of 1-butene converts to 2-butene via double-bond isomerization, with both bands coexisting. As temperature rises to 175°C, the 1640-cm^{-1} band diminishes, and the spectral center shifts to 1615 cm^{-1}, coinciding with C_5^+ product formation through carbocation-driven polymerization. By 225°C, isobutylene emerges alongside abundant C_5^+ products

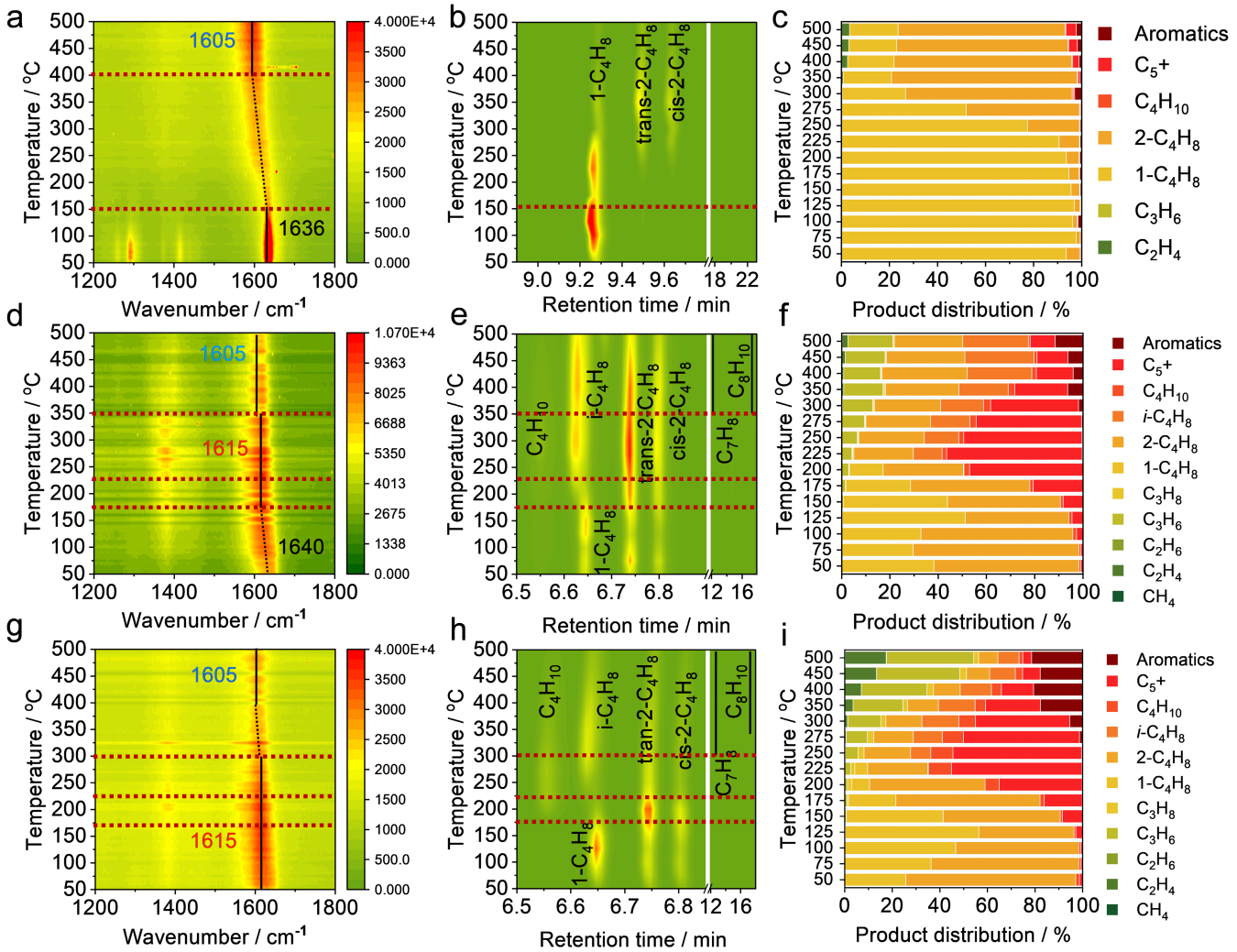

FIGURE 2 | UV-Raman spectra, corresponding gas chromatographic diagrams, and product distribution during temperature-programmed 1-butene conversion reaction over S-1 (a, b, c), ZSM-5(100) (d, e, f), and ZSM-5(38) (g, h, i).

and minor propylene (Figures 2h and S13). At 300°C, a new 1605-cm^{-1} band develops, accompanied by toluene and ethylene detection. By 350°C, xylene appears, and the 1605-cm^{-1} band surpasses 1615 cm^{-1} in intensity. At 400°C, further spectral shifts to 1605 cm^{-1} correlate with aromatic species and ethylene generation. Finally, at 500°C, concurrent catalytic cracking and aromatization yield 17% ethylene, 36% propylene, and 21% aromatics. The higher BAS density in ZSM-5(38) compared to ZSM-5(100) enhances aromatization propensity [45]. Previous studies have demonstrated that strong BAS preferentially facilitate secondary reactions of carbocationic intermediates, including hydride transfer and condensation, which in turn promote the formation of alkanes and aromatics. By contrast, weaker acid sites predominantly favor the olefin methylation/cracking pathway (olefin cycle), thereby suppressing the aromatic cycle, lowering the frequency of hydride transfer events, and consequently enhancing the propylene-to-ethylene ratio [46–48]. In the present study, the ZSM-5(100) sample exhibited a markedly higher propylene/ethylene ratio than ZSM-5(38) under identical reaction conditions, corroborating the notion that a predominance of weaker acid sites constrains the aromatic cycle and enhances propylene selectivity. Notably, the two catalysts with different Si/Al ratios did not exhibit an appreciable shift in the temperature regime required for aromatic formation, implying that the onset of the aromatic cycle is not governed solely by the density of BAS.

3.4 | Temperature-Programmed MTO Reaction Over ZSM-5 Zeolites

Operando Raman spectroscopy was employed in the mechanistic study of MTO reaction and proves highly effective for probing the mechanistic details of the reaction. During methanol conversion over ZSM-5(38), Raman spectra exhibit temperature-dependent evolution (Figures 3 and S14). Figure 3a,d reveals progressive red-shifting of Raman bands with rising temperature, correlating with shifts in product distribution and conversion rates. At temperatures below 200°C, a Raman band at ~1005 cm^{-1} corresponding to the C–O vibration was observed, which can be assigned to hydrogen-bonded methanol, indicating that methanol adsorption is the dominant process in this regime [44, 49, 50]. As the temperature increased to ~250°C, the 1005-cm^{-1} band diminished and eventually disappeared, while a new band emerged at ~1178 cm^{-1}, attributable to the methyl rock of methoxy

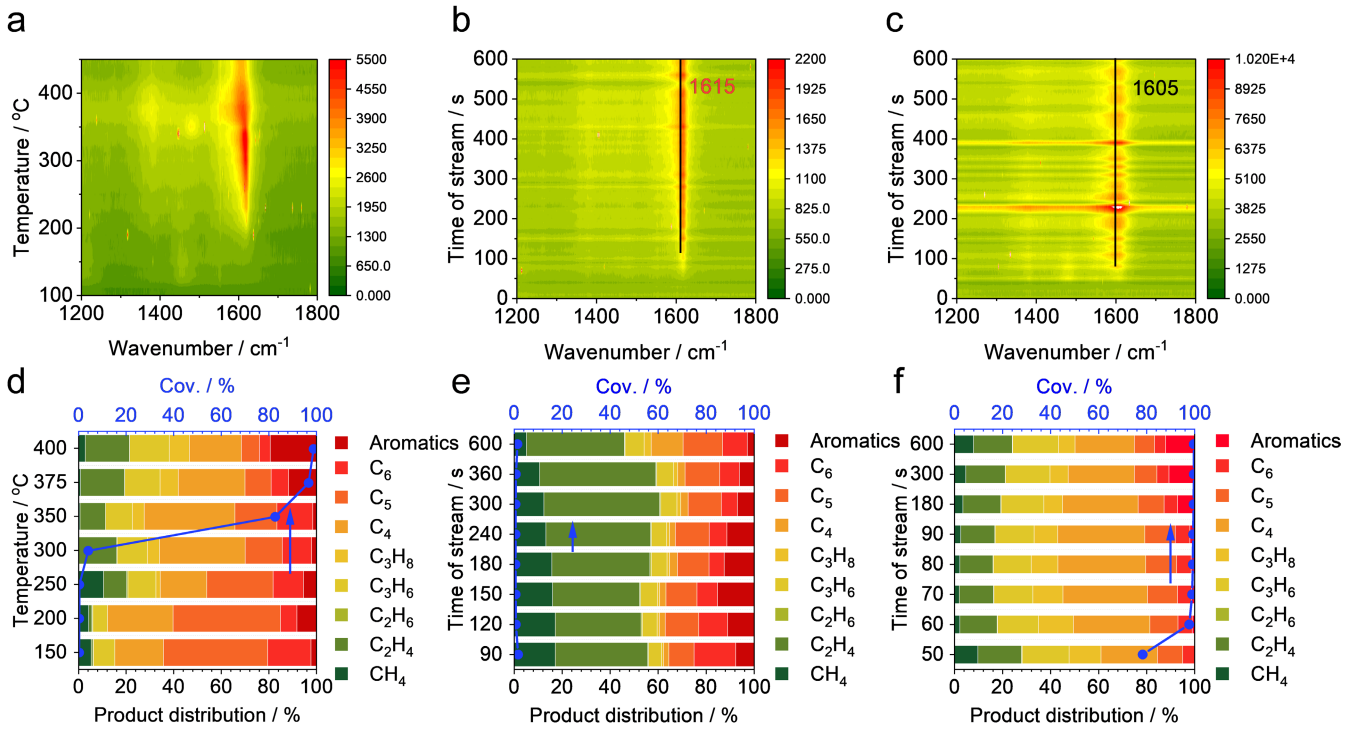

FIGURE 3 | The UV-Raman spectra and corresponding product distributions of the methanol-to-olefins reaction over ZSM-5(38) were analyzed under (a, d) temperature-programmed conditions, (b, e) at 300°C, and (c, f) at 400°C.

species, signifying the formation of surface methoxy groups. This stage is accompanied by the generation of dimethyl ether as the primary product [51–53]. Although the overall conversion remains low between 250°C and 300°C, previous studies have shown that unsaturated hydrocarbon species begin to accumulate in this temperature regime. These species, considered as precursors to polycyclic aromatic hydrocarbons (PAHs), establish the foundation for the hydrocarbon pool and contribute to the accelerated reaction kinetics observed at higher temperatures [54]. Between 300°C and 400°C, methanol conversion surges from 1% to > 99%. At 300°C, gas chromatography detects primarily methanol and dimethyl ether (< 1% conversion, Figure 3e), while the 1615-cm^{-1} Raman band signals carbocation formation (Figure 3b), marking the MTO induction period where hydrocarbon pool species accumulate. At ~350°C, a Raman band at approximately 148-cm^{-1} emerges, which can be attributed to the ring stretching vibrations of cyclopentadienyl species, suggesting the transient formation of cyclopentadiene-derived intermediates [35, 36, 55]. With further heating to 400°C, this band diminishes and ultimately disappears. Cyclopentadiene has been proposed as a crucial intermediate within the hydrocarbon pool mechanism, where it undergoes ring contraction and expansion processes that facilitate the buildup of aromatic cycles, thereby serving as a key precursor to polyaromatic hydrocarbon species [56–58]. By 400°C, methanol conversion exceeds 99%, with olefins and aromatics dominating (Figure 3f). Main hydrocarbon product shifts from C_4^+ species to propylene and aromatics over time. After 600 s, products comprise 16% ethylene, 19% propylene, and 12% aromatics, accompanied by a 1605-cm^{-1} band diagnostic of aromatic intermediates (Figure 3c). This phase represents efficient MTO conversion, where aromatic carbocations in the hydrocarbon pool mediate indirect methanol-to-olefin transformation via phenyl carbocation intermediates [59].

3.5 | Correlating the Dynamic Evolution of the Catalyst Surface to the Products Generation Through the Continuous Flow UV-Raman Reaction System

By integrating Raman spectroscopy and chromatographic analysis, we observe analogous reaction intermediates for butene and methanol conversion over ZSM-5 catalysts. The characteristic Raman band positions are governed by active carbocation species: The band center resides at 1615 cm^{-1} under olefinic carbocation dominance and shifts to 1605 cm^{-1} when aromatic carbocations prevail. Temperature critically dictates reaction selectivity by varying the carbocation formation and transformation. The Raman band appears near 1640 cm^{-1} at 50°C–150°C which is attributed to the formation of π-complexes of butene on S-1 and ZSM-5 (Scheme 1). These Raman observations are consistent with previous IR studies that reported similar adsorption states of olefins on zeolites; 1-butene initially forms π-complexes and undergoes double-bond migration on H-ZSM-5 [25, 26]. Between 50°C and 250°C, olefins undergo polymerization, cracking, and isomerization reactions on ZSM-5, with olefin carbenium ions acting as active intermediates, as evidenced by a characteristic Raman band at 1615 cm^{-1}. At elevated temperatures (300°C–400°C), aromatic carbenium ions dominate as reactive intermediates, driving the formation of aromatic compounds, with a characteristic Raman band observed at

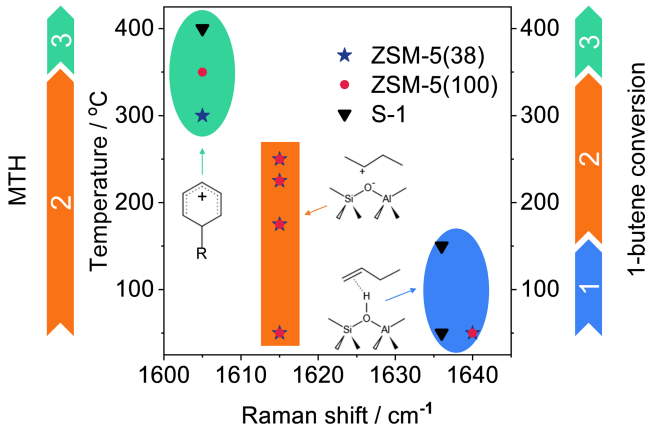

SCHEME 1 | The influence of temperature and zeolites acidity on the organics over catalyst surface detected by operando UV-Raman. Stage 1, olefin double-bond isomerization. Stage 2, the process with olefins skeleton isomerization, cracking, polymerization, and aromatization. Stage 3, generation of aromatic hydrocarbon species.

1605 cm^{-1}. These results are in line with IR reports of the progressive transformation from π-complexes to protonated species and aromatics under higher temperatures [40, 50]. The advantage of Raman spectroscopy lies in its ability to reveal the dynamic processes of carbocations, while gas chromatography is capable of separating different butene isomers and olefinic products. The combination of these two techniques simultaneously detects reactions on the catalyst surface and the formation of products provides complementary mechanistic insights for butene conversion and MTO reaction. This study underscores temperature's pivotal role in steering selectivity and highlights the synergistic power of Raman spectroscopy and gas chromatography in mechanistic elucidation of catalytic reactions.

4 | Conclusions

In summary, we developed an advanced experimental system integrating in situ Raman spectroscopy with online gas chromatography to enable real-time monitoring and mechanistic analysis of intermediate species adsorption and transformations during MFI molecular sieve-catalyzed reactions. This combined technique approach captures dynamic catalytic process evolution with unprecedented temporal resolution. Specifically, butene exhibits distinct adsorption behaviors: on BAS-free S-1, it forms physisorbed states, while on ZSM-5, it generates π-complexes. Temperature-programmed studies further delineated butene reaction pathways on MFI materials, directly linking selectivity to framework acidity. Notably, double-bond isomerization requires 200°C on S-1 (BAS-deficient) but proceeds at 50°C on acidic ZSM-5. Furthermore, ZSM-5's BAS promotes carbocation formation, driving subsequent cracking and aromatization. This system advances mechanistic understanding of molecular sieve acid catalysis, offering critical insights into reaction dynamics and selectivity control. Real-time monitoring of catalyst surface intermediates and effluent products simultaneously enhance strategy development for improved catalytic efficiency and pathway optimization.

Acknowledgments

We thank the National Key Research and Development Program of China (No. 2024YFB4105600), the National Natural Science Foundation of China (22172166, 22288101), the Youth Innovation Promotion Association CAS (2021182), the Clean Combustion and Low-Carbon Utilization of Coal, Strategic Priority Research Program of the Chinese Academy of Sciences (Grant No. XDA 29000000), and the Innovation Research Foundation of Dalian Institute of Chemical Physics, Chinese Academy of Sciences (DICP I202217) for the financial support.

Conflicts of Interest

The authors declare no conflicts of interest.

Data Availability Statement

The data that support the findings of this study are available from the corresponding author upon reasonable request.

References

1. M. Dusselier and M. E. Davis, "Small-Pore Zeolites: Synthesis and Catalysis," *Chemical Reviews* 118, no. 11 (2018): 5265–5329, https://doi.org/10.1021/acs.chemrev.7b00738.

2. E. T. C. Vogt and B. M. Weckhuysen, "Fluid Catalytic Cracking: Recent Developments on the Grand Old Lady of Zeolite Catalysis," *Chemical Society Reviews* 44, no. 20 (2015): 7342–7370, https://doi.org/10.1039/C5CS00376H.

3. J. Jae, G. A. Tompsett, A. J. Foster, et al., "Investigation Into the Shape Selectivity of Zeolite Catalysts for Biomass Conversion," *Journal of Catalysis* 279, no. 2 (2011): 257–268, https://doi.org/10.1016/j.jcat.2011.01.019.

4. Y. V. Kissin, "Chemical Mechanisms of Catalytic Cracking Over Solid Acidic Catalysts: Alkanes and Alkenes," *Catalysis Reviews* 43, no. 1–2 (2001): 85–146, https://doi.org/10.1081/CR-100104387.

5. C. M. Nguyen, B. A. De Moor, M.-F. Reyniers, and G. B. Marin, "Physisorption and Chemisorption of Linear Alkenes in Zeolites: A Combined QM-Pot (MP2//B3LYP:GULP)–Statistical Thermodynamics Study," *Journal of Physical Chemistry C* 115, no. 48 (2011): 23831–23847, https://doi.org/10.1021/jp2067606.

6. B. Yilmaz and U. Müller, "Catalytic Applications of Zeolites in Chemical Industry," *Topics in Catalysis* 52, no. 6 (2009): 888–895, https://doi.org/10.1007/s11244-009-9226-0.

7. W. Vermeiren and J.-P. Gilson, "Impact of Zeolites on the Petroleum and Petrochemical Industry," *Topics in Catalysis* 52, no. 9 (2009): 1131–1161, https://doi.org/10.1007/s11244-009-9271-8.

8. N. Rahimi and R. Karimzadeh, "Catalytic Cracking of Hydrocarbons Over Modified ZSM-5 Zeolites to Produce Light Olefins: A Review," *Applied Catalysis. A, General* 398, no. 1 (2011): 1–17, https://doi.org/10.1016/j.apcata.2011.03.009.

9. P. Tian, Y. Wei, M. Ye, and Z. Liu, "Methanol to Olefins (MTO): From Fundamentals to Commercialization," *ACS Catalysis* 5, no. 3 (2015): 1922–1938, https://doi.org/10.1021/acscatal.5b00007.

10. F. Joensen, P. E. H. Nielsen, and M. D. Palis Sørensen, "Biomass to Green Gasoline and Power," *Biomass Conversion and Biorefinery* 1, no. 2 (2011): 85–90, https://doi.org/10.1007/s13399-011-0008-0.

11. T. Mole, J. A. Whiteside, and D. Seddon, "Aromatic Co-Catalysis of Methanol Conversion Over Zeolite Catalysts," *Journal of Catalysis* 82, no. 2 (1983): 261–266, https://doi.org/10.1016/0021-9517(83)90192-6.

12. A. Sassi, M. A. Wildman, H. J. Ahn, P. Prasad, J. B. Nicholas, and J. F. Haw, "Methylbenzene Chemistry on Zeolite HBeta:

Multiple Insights Into Methanol-to-Olefin Catalysis," *Journal of Physical Chemistry B* 106, no. 9 (2002): 2294–2303, https://doi.org/10.1021/jp013392k.

13. D. Lesthaeghe, V. V. Speybroeck, and M. Waroquier, "Theoretical Evaluation of Zeolite Confinement Effects on the Reactivity of Bulky Intermediates," *Physical Chemistry Chemical Physics* 11, no. 26 (2009): 5222–5226, https://doi.org/10.1039/B902364J.

14. J. Zhong, J. Han, Y. Wei, and Z. Liu, "Catalysts and Shape Selective Catalysis in the Methanol-to-Olefin (MTO) Reaction," *Journal of Catalysis* 396 (2021): 23–31, https://doi.org/10.1016/j.jcat.2021.01.027.

15. V. Nieminen, M. Sierka, D. Y. Murzin, and J. Sauer, "Stabilities of C3–C5 Alkoxide Species Inside H-FER Zeolite: A Hybrid QM/MM Study," *Journal of Catalysis* 231, no. 2 (2005): 393–404, https://doi.org/10.1016/j.jcat.2005.01.035.

16. J. N. Kondo, F. Wakabayashi, and K. Domen, "IR Study of Adsorption of Olefins on Deuterated ZSM-5," *Journal of Physical Chemistry B* 102, no. 12 (1998): 2259–2262, https://doi.org/10.1021/jp9800416.

17. A. Bhan, Y. V. Joshi, W. N. Delgass, and K. T. Thomson, "DFT Investigation of Alkoxide Formation From Olefins in H-ZSM-5," *Journal of Physical Chemistry B* 107, no. 38 (2003): 10476–10487, https://doi.org/10.1021/jp034382h.

18. S. Schallmoser, G. L. Haller, M. Sanchez-Sanchez, and J. A. Lercher, "Role of Spatial Constraints of Brønsted Acid Sites for Adsorption and Surface Reactions of Linear Pentenes," *Journal of the American Chemical Society* 139, no. 25 (2017): 8646–8652, https://doi.org/10.1021/jacs.7b03690.

19. Y. Wang, J. Han, N. Wang, et al., "Conversion of Methanol to Propylene Over SAPO-14: Reaction Mechanism and Deactivation," *Chinese Journal of Catalysis* 43, no. 8 (2022): 2259–2269, https://doi.org/10.1016/S1872-2067(22)64123-8.

20. B. Manookian, E. D. Hernandez, M. D. Baer, C. J. Mundy, F. C. Jentoft, and S. M. Auerbach, "Experimental and DFT Calculated IR Spectra of Guests in Zeolites: Acyclic Olefins and Host–Guest Interactions," *Journal of Physical Chemistry C* 124, no. 19 (2020): 10561–10572, https://doi.org/10.1021/acs.jpcc.0c01225.

21. Q. Ren, M. Rybicki, and J. Sauer, "Interaction of C3–C5 Alkenes With Zeolitic Brønsted Sites: π-Complexes, Alkoxides, and Carbenium Ions in H-FER," *Journal of Physical Chemistry C* 124, no. 18 (2020): 10067–10078, https://doi.org/10.1021/acs.jpcc.0c03061.

22. P. N. Plessow and F. Studt, "How Accurately Do Approximate Density Functionals Predict Trends in Acidic Zeolite Catalysis?," *Journal of Physical Chemistry Letters* 11, no. 11 (2020): 4305–4310, https://doi.org/10.1021/acs.jpclett.0c01240.

23. J. Hajek, J. Van der Mynsbrugge, K. De Wispelaere, et al., "On the Stability and Nature of Adsorbed Pentene in Brønsted Acid Zeolite H-ZSM-5 at 323 K," *Journal of Catalysis* 340 (2016): 227–235, https://doi.org/10.1016/j.jcat.2016.05.018.

24. M. John, K. Alexopoulos, M.-F. Reyniers, and G. B. Marin, "Effect of Zeolite Confinement on the Conversion of 1-Butanol to Butene Isomers: Mechanistic Insights From DFT Based Microkinetic Modelling," *Catalysis Science & Technology* 7, no. 14 (2017): 2978–2997, https://doi.org/10.1039/C7CY00536A.

25. J. N. Kondo, S. Liqun, F. Wakabayashi, and K. Domen, "IR Study of Adsorption and Reaction of 1-Butene on H-ZSM-5," *Catalysis Letters* 47, no. 2 (1997): 129–133, https://doi.org/10.1023/A:1019096703066.

26. J. N. Kondo, L. Shao, F. Wakabayashi, and K. Domen, "Doublebond Migration of an Olefin Without Protonated Species on H(D) Form Zeolites," *Journal of Physical Chemistry B* 101, no. 45 (1997): 9314–9320, https://doi.org/10.1021/jp971812t.

27. P. Cnudde, K. De Wispelaere, J. der Van Mynsbrugge, M. Waroquier, and V. Van Speybroeck, "Effect of Temperature and Branching on the Nature and Stability of Alkene Cracking Intermediates in H-ZSM-5," *Journal of Catalysis* 345 (2017): 53–69, https://doi.org/10.1016/j.jcat.2016.11.010.

28. M. Signorile, F. Bonino, A. Damin, and S. Bordiga, "In Situ Resonant UV-Raman Spectroscopy of Polycyclic Aromatic Hydrocarbons," *Journal of Physical Chemistry C* 119, no. 21 (2015): 11694–11698, https://doi.org/10.1021/acs.jpcc.5b02209.

29. S. Bordiga, C. Lamberti, F. Bonino, A. Travert, and F. Thibault-Starzyk, "Probing Zeolites by Vibrational Spectroscopies," *Chemical Society Reviews* 44, no. 20 (2015): 7262–7341, https://doi.org/10.1039/C5CS00396B.

30. P. Beato, E. Schachtl, K. Barbera, F. Bonino, and S. Bordiga, "Operando Raman Spectroscopy Applying Novel Fluidized Bed Micro-Reactor Technology," *Catalysis Today* 205 (2013): 128–133, https://doi.org/10.1016/j.cattod.2012.09.030.

31. M. Signorile, D. Rojo-Gama, F. Bonino, P. Beato, S. Svelle, and S. Bordiga, "Topology-Dependent Hydrocarbon Transformations in the Methanol-to-Hydrocarbons Reaction Studied by Operando UV-Raman Spectroscopy," *Physical Chemistry Chemical Physics* 20, no. 41 (2018): 26580–26590, https://doi.org/10.1039/C8CP04240C.

32. F. Fan, Z. Feng, and C. Li, "UV Raman Spectroscopic Studies on Active Sites and Synthesis Mechanisms of Transition Metal-Containing Microporous and Mesoporous Materials," *Accounts of Chemical Research* 43, no. 3 (2010): 378–387, https://doi.org/10.1021/ar900210g.

33. P. C. Stair, "The Application of UV Raman Spectroscopy for the Characterization of Catalysts and Catalytic Reactions," in *Advances in Catalysis*, eds. B. Gates and H. Knozinger (Academic Press, 2007), 75–98, https://doi.org/10.1016/S0360-0564(06)51002-8.

34. I. Lezcano-Gonzalez, E. Campbell, A. E. J. Hoffman, et al., "Insight Into the Effects of Confined Hydrocarbon Species on the Lifetime of Methanol Conversion Catalysts," *Nature Materials* 19, no. 10 (2020): 1081–1087, https://doi.org/10.1038/s41563-020-0800-y.

35. Y. T. Chua and P. C. Stair, "An Ultraviolet Raman Spectroscopic Study of Coke Formation in Methanol to Hydrocarbons Conversion Over Zeolite H-MFI," *Journal of Catalysis* 213, no. 1 (2003): 39–46, https://doi.org/10.1016/S0021-9517(02)00026-X.

36. J. Li, G. Xiong, Z. Feng, Z. Liu, Q. Xin, and C. Li, "Coke Formation During the Methanol Conversion to Olefins in Zeolites Studied by UV Raman Spectroscopy," *Microporous and Mesoporous Materials* 39, no. 1 (2000): 275–280, https://doi.org/10.1016/S1387-1811(00)00204-3.

37. E. Campbell, I. V. Sazanovich, M. Towrie, M. J. Watson, I. Lezcano-Gonzalez, and A. M. Beale, "Methanol-to-Olefins Studied by UV Raman Spectroscopy as Compared to Visible Wavelength: Capitalization on Resonance Enhancement," *Journal of Physical Chemistry Letters* 15, no. 26 (2024): 6826–6834, https://doi.org/10.1021/acs.jpclett.4c00865.

38. M. Signorile, D. Rojo Gama, F. Bonino, S. Svelle, P. Beato, and S. Bordiga, "Operando UV-Raman Study of the Methanol to Olefins Reaction Over SAPO-34: Spatiotemporal Evolution Monitored by Different Reactor Approaches," *Catalysis Today* 336 (2019): 203–209, https://doi.org/10.1016/j.cattod.2018.11.065.

39. P. M. Allotta and P. C. Stair, "Time-Resolved Studies of Ethylene and Propylene Reactions in Zeolite H-MFI by In-Situ Fast IR Heating and UV Raman Spectroscopy," *ACS Catalysis* 2, no. 11 (2012): 2424–2432, https://doi.org/10.1021/cs3004215.

40. T. Armaroli, E. Finocchio, G. Busca, and S. Rossini, "A FT-IR Study of the Adsorption of C5 Olefinic Compounds on NaX Zeolite," *Vibrational Spectroscopy* 20, no. 1 (1999): 85–94, https://doi.org/10.1016/S0924-2031(99)00024-7.

41. Course Notes on the Interpretation of Infrared and Raman Spectra By D. W. Mayo, F. A. Miller, and R. W. Hannah, "(Bowdoin College, University of Pittsburgh, Bowdoin College, Respectively). Wiley-Interscience, Hoboken. 2004. Xxvi +567 Pp. 16 × 24 Cm. $125.00. ISBN 0–471–24823-1," *Journal of Natural Products* 67, no. 10 (2004): 1775, https://doi.org/10.1021/np030756m.

42. M. John, K. Alexopoulos, M.-F. Reyniers, and G. B. Marin, "Reaction Path Analysis for 1-Butanol Dehydration in H-ZSM-5 Zeolite: Ab Initio and Microkinetic Modeling," *Journal of Catalysis* 330 (2015): 28–45, https://doi.org/10.1016/j.jcat.2015.07.005.

43. W. Chen, X. Yi, Z. Liu, X. Tang, and A. Zheng, "Carbocation Chemistry Confined in Zeolites: Spectroscopic and Theoretical Characterizations," *Chemical Society Reviews* 51, no. 11 (2022): 4337–4385, https://doi.org/10.1039/D1CS00966D.

44. H. An, F. Zhang, Z. Guan, X. Liu, F. Fan, and C. Li, "Investigating the Coke Formation Mechanism of H-ZSM-5 During Methanol Dehydration Using Operando UV–Raman Spectroscopy," *ACS Catalysis* 8, no. 10 (2018): 9207–9215, https://doi.org/10.1021/acscatal.8b00928.

45. M. Bjørgen, S. Svelle, F. Joensen, et al., "Conversion of Methanol to Hydrocarbons Over Zeolite H-ZSM-5: On the Origin of the Olefinic Species," *Journal of Catalysis* 249, no. 2 (2007): 195–207, https://doi.org/10.1016/j.jcat.2007.04.006.

46. C. D. Chang, C. T.-W. Chu, and R. F. Socha, "Methanol Conversion to Olefins Over ZSM-5: I. Effect of Temperature and Zeolite SiO2Al2O3," *Journal of Catalysis* 86, no. 2 (1984): 289–296, https://doi.org/10.1016/0021-9517(84)90374-9.

47. M. Khanmohammadi, S. Amani, A. B. Garmarudi, and A. Niaei, "Methanol-to-Propylene Process: Perspective of the Most Important Catalysts and Their Behavior," *Chinese Journal of Catalysis* 37, no. 3 (2016): 325–339, https://doi.org/10.1016/S1872-2067(15)61031-2.

48. H. Huang, C. Yuan, P. Zhong, et al., "One-Step Synthesis of High-Silica ZSM-5 Zeolite With Less Internal Silicon Hydroxyl Groups: Highly Stable Catalyst for Methanol to Propene Reaction," *Catalysis Letters* 152, no. 7 (2022): 2178–2185, https://doi.org/10.1007/s10562-021-03796-1.

49. S. K. Matam, R. F. Howe, A. Thetford, and C. R. A. Catlow, "Room Temperature Methoxylation in Zeolite H-ZSM-5: An Operando DRIFTS/Mass Spectrometric Study," *Chemical Communications* 54, no. 91 (2018): 12875–12878, https://doi.org/10.1039/C8CC07444E.

50. A. Zachariou, A. P. Hawkins, R. F. Howe, et al., "A Spectroscopic Paradox: The Interaction of Methanol With ZSM-5 at Room Temperature," *Topics in Catalysis* 64, no. 9 (2021): 672–684, https://doi.org/10.1007/s11244-021-01462-9.

51. M. Jayamurthy and S. Vasudevan, "Methanol-to-Gasoline (MTG) Conversion Over ZSM-5. A Temperature Programmed Surface Reaction Study," *Catalysis Letters* 36, no. 1 (1996): 111–114, https://doi.org/10.1007/BF00807214.

52. Suwardiyanto, R. F. Howe, E. K. Gibson, et al., "An Assessment of Hydrocarbon Species in the Methanol-to-Hydrocarbon Reaction Over a ZSM-5 Catalyst," *Faraday Discussions* 197, no. 0 (2017): 447–471, https://doi.org/10.1039/C6FD00195E.

53. A. Zachariou, A. Hawkins, S. F. Parker, D. Lennon, and R. F. Howe, "Neutron Spectroscopy Studies of Methanol to Hydrocarbons Catalysis Over ZSM-5," *Catalysis Today* 368 (2021): 20–27, https://doi.org/10.1016/j.cattod.2020.05.030.

54. H. Schulz, ""Coking" of Zeolites During Methanol Conversion: Basic Reactions of the MTO-, MTP- and MTG Processes," *Catalysis Today* 154, no. 3 (2010): 183–194, https://doi.org/10.1016/j.cattod.2010.05.012.

55. E. D. Hernandez and F. C. Jentoft, "Spectroscopic Signatures Reveal Cyclopentenyl Cation Contributions in Methanol-to-Olefins Catalysis," *ACS Catalysis* 10, no. 10 (2020): 5764–5782, https://doi.org/10.1021/acscatal.0c00721.

56. W. Zhang, S. Xu, Y. Zhi, Y. Wei, and Z. Liu, "Methylcyclopentenyl Cation Mediated Reaction Route in Methanol-to-Olefins Reaction Over H-RUB-50 With Small Cavity," *Journal of Energy Chemistry* 45 (2020): 25–30, https://doi.org/10.1016/j.jechem.2019.09.022.

57. W. Zhang, Y. Zhi, J. Huang, et al., "Methanol to Olefins Reaction Route Based on Methylcyclopentadienes as Critical Intermediates," *ACS Catalysis* 9, no. 8 (2019): 7373–7379, https://doi.org/10.1021/acscatal.9b02487.

58. M. Zhang, S. Xu, Y. Wei, et al., "Changing the Balance of the MTO Reaction Dual-Cycle Mechanism: Reactions Over ZSM-5 With Varying Contact Times," *Chinese Journal of Catalysis* 37, no. 8 (2016): 1413–1422, https://doi.org/10.1016/S1872-2067(16)62466-X.

59. X. Wu, S. Xu, Y. Wei, et al., "Evolution of C–C Bond Formation in the Methanol-to-Olefins Process: From Direct Coupling to Autocatalysis," *ACS Catalysis* 8, no. 8 (2018): 7356–7361, https://doi.org/10.1021/acscatal.8b02385.

Supporting Information

Additional supporting information can be found online in the Supporting Information section. **Figure S1:** Integrated system of continuous-flow UV-Raman with 16-position GC autosampler. **Figure S2:** XRD pattern of S-1, ZSM-5(100), and ZSM-5(38). **Figure S3:** NH_3-TPD profile of S-1, ZSM-5(100), and ZSM-5(38). **Figure S4:** IR profile of S-1, ZSM-5(100), and ZSM-5(38). **Figure S5:** SEM images of S-1. **Figure S6:** SEM images of ZSM-5(100). **Figure S7:** SEM images of ZSM-5(38). **Figure S8:** UV-Raman spectra during temperature-programmed 1-butene conversion reaction over S-1. **Figure S9:** UV-Raman spectra of 1-butanol (red, after 180-s exposure) and 1-butene (black, after 300-s exposure) adsorbed on S-1 at 50°C. **Figure S10:** UV-Raman spectra of 1-butanoland 1-butene adsorbed on ZSM-5(38) at 50°C. **Figure S11:** UV-Raman spectra during temperature-programmed 1-butene conversion reaction over S-1. **Figure S12:** UV-Raman spectra during temperature-programmed 1-butene conversion reaction over ZSM-5(100). **Figure S13:** UV-Raman spectra during temperature-programmed 1-butene conversion reaction over ZSM-5(38). **Figure S14:** UV-Raman spectra during temperature-programmed 1-butene conversion reaction over ZSM-5(38). **Figure S15:** Adsorption of i-butene and 1-butanol on ZSM-5(100) at 50°C. **Table S1:** The elemental content of S-1 measured by XRF. **Table S2:** The elemental content of ZSM-5(100) measured by XRF. **Table S3:** The elemental content of ZSM-5(38) measured by XRF.